

# Stationarity Region of Mm-Wave Channel Based on Outdoor Microcellular Measurements at 28 GHz

R. Wang<sup>1</sup>, *Student Member, IEEE*, C. U. Bas<sup>1</sup>, *Student Member, IEEE*,  
S. Sangodoyin<sup>1</sup>, *Student Member, IEEE*, S. Hur<sup>2</sup>, *Member, IEEE*,  
J. Park<sup>2</sup>, *Member, IEEE*, J. Zhang<sup>3</sup>, *Fellow, IEEE*, A. F. Molisch<sup>1</sup>, *Fellow, IEEE*

<sup>1</sup>University of Southern California, Los Angeles, CA USA,

<sup>2</sup>Samsung Electronics, Suwon, Korea,

<sup>3</sup>Samsung Research America, Richardson, TX, USA

**Abstract**—The stationarity region, i.e., the area in which the statistics of a propagation channel remain constant, is an important measure of the propagation channel, and essential for efficient system design. This paper presents what is to our knowledge the first extensive measurement campaign for measuring the stationarity region of MIMO mm-wave channels. Using a novel 28 GHz phased-array sounder with high phase stability, we present results in an urban microcell LoS, and LOS to NLOS transition region scenario, for the stationarity region of shadowing, power delay profile, and the angular power spectrum. A comparison to results at cm-waves shows considerably reduced stationarity region size, which has an important impact on system design.

## I. INTRODUCTION

One of the most important ways to satisfy the constantly increasing demand for wireless data is making available more spectrum for cellular and WLAN communications. An especially promising frequency range is the millimeter-wave (mm-wave) band, due to the large swaths of currently fallow spectrum [1]. In the USA, the frequency regulator (Federal Communications Commission, FCC) has recently made available more than 15 GHz of bandwidth for unlicensed or licensed operation, and other countries, as well as the World Radio Conference, are expected to follow suit. Furthermore, recent progress in semiconductor technology and adaptive beamforming has made possible the fabrication of mm-wave hardware at reasonable prices [2]. For all these reasons, the 5G standard by 3GPP (the international standardization body for cellular communications) as well as the IEEE 802.11 standard for WLANs prominently feature mm-wave communications.

In order to design and evaluate wireless systems, a thorough understanding of the propagation channel is required [3]. In this context, it is important to note that mm-wave channels show fundamentally different behavior compared to channels below 6 GHz carrier frequency, which have been mostly investigated up to now. These differences are an almost complete absence of diffraction as effective propagation process, and the relatively greater roughness (in units of wavelength) of objects the waves interact with [4]. For these reasons, a number of propagation measurements have been done in both indoor and outdoor environments at mm-waves over the past 30 years (see [4]–[6] for a review and further references. Recent work has particularly concentrated on directional channel

characteristics, i.e., the channel behavior as seen by directional antennas since use of directional antennas is essential at mm-wave frequencies as the antenna gain is required to compensate for the higher free-space pathloss (PL). Standardized channel models for IEEE 802.11ad [7] and 3GPP SCM [8] have been derived. Small-scale fading statistics have been analyzed, e.g., in [9].

However, despite the existence of some measurements, many gaps in our understanding of propagation channels remain. One of the most important gaps is the *dynamic* behavior of the channels. Our results attempt to answer the question about the *stationarity region* of the channel, i.e., the area over which the *channel statistics* stay approximately constant. This is so important for mm-wave systems because on one hand due to the mobility of users, fixed-orientation horn or parabolic antennas cannot be used in cellular systems and on the other hand, adaptive beamforming is often based on the channel statistics (and not the instantaneous fading) in order to reduce channel training overhead and hardware requirements [10]. Furthermore, the area in which the power delay profile (PDP) / delay spread stays constant is critical for efficient pilot design, while gain control and similar parameters may depend on the shadowing state. For all these reasons, measurements of the stationarity region size is essential. At cm-wave frequencies, numerous investigations of stationarity region size have been done, and metrics have been established to measure the stationarity region size of shadowing, PDP, and correlation matrix distance (CMD) [11]–[13] and references therein.

Yet, at mm-wave frequencies, hardly any measurements exist, with the exception of the few cases discussed below. For example, the corresponding parameters in the 3GPP channel model are not based on measurements at mm-wave frequencies. Ref. [14] investigates the lifetime of multipath components in a street canyon, as well as their change in power and direction. However, the measurements were only done in a line-of-sight (LoS) scenario in a single street canyon, measured at 7 locations separated by 5 m each, and furthermore are single input multiple output (SIMO), not multiple-input multiple-output (MIMO). Also, measurements were evaluated with respect to the persistence and angle change of individual multipath components, which are only indirectly related to

stationarity regions. Some recent work [15]–[17], done in parallel to our investigations, investigates the nonstationary statistics of mm-wave channel, which include the diffraction measurement and the transition between LoS and non-line-of-sight (NLoS), but is based on experiments at 73 GHz, in contrast to our investigations at 28 GHz. Results are presented for the change in the pathloss along a track, or in a cluster, with measurement locations spaced 5 m apart. However, to our knowledge there are no measurements in the literature that are based on a dense spatial sampling; nor are there measurements of stationarity regions for shadowing, PDP, or angular spectra. In this paper, we aim to fill this gap.

The main contributions of this paper are as follows:

- We present the measurement setup and procedure for MIMO measurements on a *densely sampled* route, using a novel phase array based channel sounder with high phase stability. Our results are based on more than 29 million recorded impulse responses.
- For measurement routes covering LoS and the transition between LoS and NLoS, we present stationarity regions of channel statistics such as PDP and shadow fading, as well as the evolution of angular spectra.

The results thus serve as important guidelines for mm-wave system design.

The remainder of the paper is organized as follows: Section II describes our channel sounder and the measurement environment and procedure. Section III covers the evaluation procedure of the data, and presents the results. A summary and conclusions in Section IV wrap up the paper.

## II. MEASUREMENT CAMPAIGN

In this campaign, we used a real-time, phased-array, wide-band mm-wave channel sounder that is capable of beam-forming at both the receiver (RX) and the transmitter (TX) [18]. Both the TX and the RX are equipped with phased antenna arrays capable of forming beams which can be electronically steered with  $5^\circ$  resolution in the range of  $[-45^\circ, 45^\circ]$  in azimuth. Compared to the setups with rotating horn antennas or virtual antenna arrays, the electronically switched beams decreases the measurement time for one RX-TX location from hours to milliseconds. During this campaign, we measured for 361 total beam pairs in 14.44 ms per location, with a single-input single-output (SISO) averaging factor of 10 allowing a measurable path-loss of 169 dB. Thanks to the short measurement time, unlike the rotating horn antenna sounders, we can perform double directional measurements on continuous routes as the RX or TX moves. By using GPS-disciplined Rubidium frequency references, we were able to achieve both short-time and long-time phase stability. Combined with the short measurement time this limits the phase drift between TX and RX even when they are physically separated and have no cabled connection for synchronization as in this case. Consequently, all TX and RX beams were measured phase-coherently.

The sounding signal has 801 tones equally spaced over 400 MHz total bandwidth. This provides a 2.5 ns delay res-

TABLE I  
SOUNDER SPECIFICATIONS

Hardware Specifications	
Center Frequency	27.85 GHz
Instantaneous Bandwidth	400 MHz
Antenna array size	8 by 2 (for both TX and RX)
Horizontal beam steering	$-45^\circ$ to $45^\circ$
Horizontal 3dB beam width	$12^\circ$
Horizontal steering steps	$5^\circ$
Beam switching speed	$2 \mu\text{s}$
TX EIRP	57 dBm
RX noise figure	$\leq 5$ dB
ADC/AWG resolution	10/15-bit
Data streaming speed	700 MBps
Sounding Waveform Specifications	
Waveform duration	$2 \mu\text{s}$
Repetition per beam pair	10
Number of tones	801
Tone spacing	500 kHz
PAPR	0.4 dB
Total sweep time	14.44 ms
MIMO repetition rate	5 Hz

olution with  $2 \mu\text{s}$  measurable excess delay. To better utilize the dynamic range of the sounder, the phases of individual tones are manipulated as suggested in [19] resulting in a peak to average power ratio (PAPR) of 0.4 dB. The main specifications for the sounder and sounding signal are listed in Table I. With the flexible FPGA control interface, many of these operation parameters such as; the number of and the order of TX-RX beam pairs, the SISO duration and the number of SISO repetition per beam pair, the measurable excess delay and the MIMO repetition rate can be modified on a per campaign basis. For example, for measurements in highly dynamic environments, we can use only the odd numbered beams (without missing any multi-path components, since the beam width is larger than twice the beam step) with no SISO averaging, and lower the measurement time for a MIMO sweep to  $400 \mu\text{s}$ . Further details of the sounder and the validation measurements can be found in [18].

The measurements were performed on the University Park Campus, University of Southern California, in Los Angeles, CA, USA, in an area that resembles a typical urban environment. The TX was placed on a scissor lift at the height of 5 m while the RX was on a mobile cart with the antenna height of 1.8 m. We captured one MIMO snapshot every 200 ms as we moved the RX with an approximate speed of 0.15 m/s on straight lines resulting in a spatial sampling with an average rate of 3 cm per sample. As the RX moves, a laser distance meter records the distance to a reference object placed at the start of the route.

We focused on two scenarios; LoS and LoS to NLoS transition. For all measurements we performed  $[-45^\circ, 45^\circ]$  azimuth sweeps at both the RX and the TX, while the bore-sights of the arrays facing towards to possible paths of propagation. The LoS measurements cover a 160 m route, and in this case  $90^\circ$  RX sector was facing  $0^\circ$ . The LoS to NLoS transition

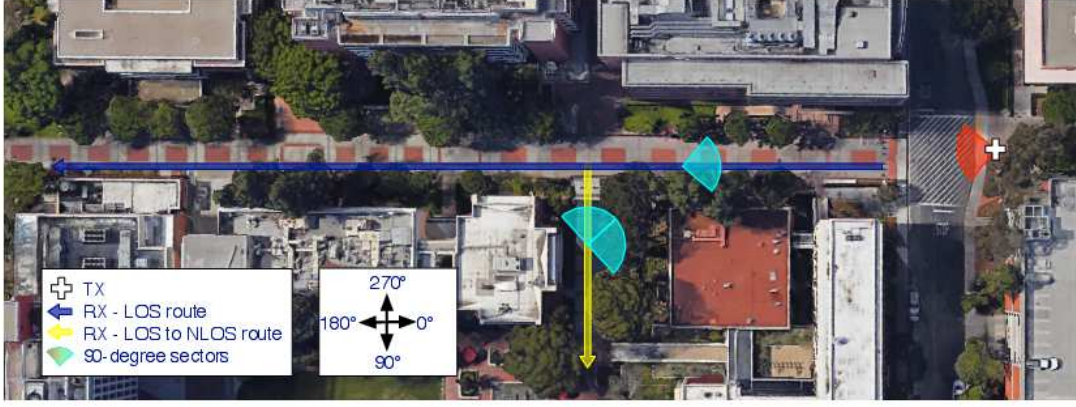


Fig. 1. Measurement Environment

measurements were captured on a 40 m route which starts from 53 m into the LoS route. For the transition, we did two runs to include both when the RX sector is oriented at  $0^\circ$  (i.e. same orientation with LoS) and  $270^\circ$  (i.e. facing towards the LoS route). All routes along with RX/TX orientations are depicted in Figure 1.

### III. EVALUATION

#### A. Data postprocessing

The directional PDP is estimated from the measured transfer function  $H$  according to

$$P_h(m, n, x, \tau) = |\mathcal{F}^{-1}\{w(f)H(m, n, x, f)\}|^2, \quad (1)$$

where  $m = 1, 2, \dots, M_t$  is the TX beam index,  $n = 1, 2, \dots, M_r$  is the RX beam index, and  $x$  is the displacement of RX from the origin of the continuous route. A gain-corrected Hanning window  $w(f)$  is applied on the transfer function  $H$  before taking inverse fourier transform (IFFT). We have also compensated the transfer function based on the system calibration response.

Thanks to the precise laser distance meter, we can compute the average PDP over small-scale fading in a distance window with length  $d_0 = 40$  cm, which is approximately  $40\lambda$  at 28 GHz. The  $i$ th average PDP is given by

$$\bar{P}_h(m, n, i, \tau) = \frac{1}{N_i} \sum_{x \in D_i} P_h(m, n, x, \tau), \quad (2)$$

where  $D_i = [(i-1)d_0, i \cdot d_0)$ ,  $N_i$  is the number of MIMO snapshots taken during this distance window  $D_i$ .

Similar to the spirit of [18], [20], the omni-directional<sup>1</sup> PDP is computed as

$$\bar{P}_{h,\max}(i, \tau) = \max_{m,n} \bar{P}_h(m, n, i, \tau). \quad (3)$$

As a result the received power can be computed by

$$P_{RX}(d_i) = \sum_{\tau \in S_{\tau,i}} \bar{P}_{h,\max}(i, \tau), \quad (4)$$

<sup>1</sup>Strictly speaking the result can only be applied to the  $90^\circ$  openings at both TX and RX

TABLE II  
PARAMETERS OF THE PATHLOSS MODEL FOR THE LOS AND LOS TO NLOS TRANSITION SCENARIOS

Parameters	Values
$n_1$	2.36
$n_2$	11.93
$b$	63.18
$d_c$	139.64
$n_{tr}$	2.59
$\Delta$	0

where  $S_{\tau,i}$  is the set of delay bins whose power is 3 dB higher than the noise floor in  $\bar{P}_{h,\max}(i, \tau)$ . The propagation loss in dB is then given as

$$PL(d_i) = P_t - 10\log_{10}(P_{RX}(d_i)), \quad (5)$$

where  $P_t$  is the transmit power and kept at constant during the experiments.

#### B. Pathloss fitting

Fig. 2 presents the pathloss fitting result for the LoS route. Due to the foliage effect, the received power for the tail of the LoS route is significantly attenuated.<sup>2</sup> The results demonstrate the importance of including foliage effect in mm-wave system simulations. We fit the propagation loss data to a dual-slope model to acquire the pathloss exponents ( $n_1, n_2$ ), cut-off distance  $d_c$  and the intercept offset  $b$ . The fitting model is given as

$$\overline{PL}_{\text{los}}(d) = \begin{cases} 10n_1 \log_{10}(d) + b, & \text{if } d < d_c \\ 10n_1 \log_{10}(d_c) + 10n_2 \log_{10}(\frac{d}{d_c}) + b, & \text{otherwise} \end{cases} \quad (6)$$

where  $d$  is the distance between TX and RX. The fitted parameters are listed in Tab. II.

The realization of the shadowing process is the residual component of this fitting process, thus determined by

$$Sh(d_i) = PL(d_i) - \overline{PL}_{\text{los}}(d_i) \quad (7)$$

<sup>2</sup>Note that this is *not* a breakpoint due to the classical ground reflection model - that breakpoint is at 10 km.

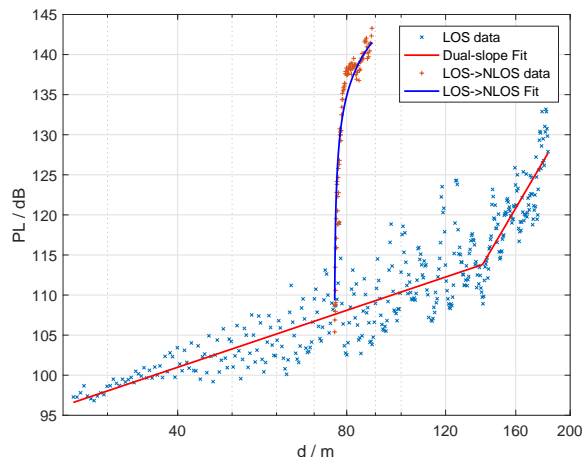


Fig. 2. The fitting of pathloss data, LoS data based on a dual-slope model given by Eq. (6), LoS→NLoS data based on the street-by-street PL model in [21]

Let us investigate the shadowing process of measurement points that experience an unobstructed LoS, i.e.  $d < d_c$ . Assuming the shadowing process is stationary during this part of the route, the autocorrelation function of the shadowing process can be evaluated according to

$$A_{Sh}(\Delta d) = \frac{\mathbb{E}_d\{Sh(d)Sh(d + \Delta d)\}}{\mathbb{E}_d\{Sh^2(d)\}}, \quad (8)$$

where  $\mathbb{E}\{\}$  is the expectation operator. The standard deviation of shadowing is 3.11 dB, and the autocorrelation distance is 1.2 m when we set the decorrelation threshold as  $1/e$ . The relatively short shadowing correlation distance can be explained by the oscillation of propagation loss around the mean path loss, which is illustrated in Fig. 3. This phenomenon is also observed in the typical two-path channel [3]. While interference between multipath components is normally not counted as “shadowing”, it could be eliminated here only by using a larger averaging window, which would entail the danger of averaging out some actual shadowing as well. This is a demonstration of the general difficulty of separating small-scale and large-scale fading, an effect that occurs at all frequencies [22].

We also analyze the propagation loss for the LoS-to-NLoS transition route, where RX has two orientations. Let us denote them as  $PL_{tr,1}(y)$  and  $PL_{tr,2}(y)$ , where the subscript 1 and 2 is used to differentiate the two routes measured for LoS to NLoS transition. We analyze the smaller propagation loss at the same location, which is defined as

$$PL_{tr}(y) = \min_{i \in \{1,2\}} PL_{tr,i}(y) \quad (9)$$

We observe a large and rapid increase of propagation loss when RX moves from LoS to NLoS. The path loss increase is about 30 dB, which is close to the 25 dB reported in [17]. Following the method in [21], we propose to fit this LoS to NLoS transition part according to the model given by

$$PL_{tr}(y) = 10n_{tr}\log_{10}(y) + \Delta + \overline{PL}_{los}(d_1) \quad (10)$$

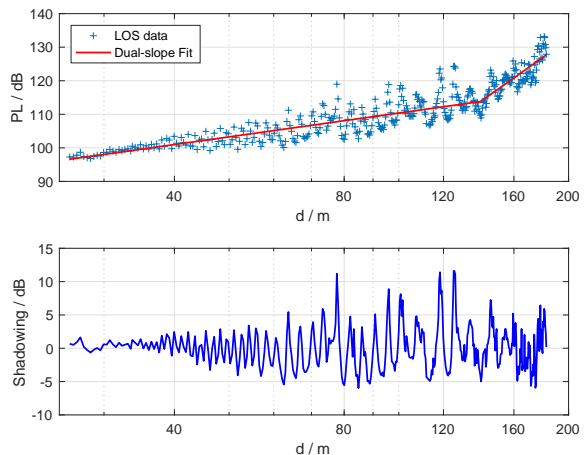


Fig. 3. The shadowing realization extracted from the LoS route

Here  $y$  is the local displacement of RX from the starting point of the transition route,  $\Delta$  denotes the corner loss proposed in [21] and is constrained to be nonnegative during the data fitting, and finally  $d_1$  the distance between the route starting point and TX. The corresponding measured data and the fitted line is presented in Fig. 2, and the parameters are given in Tab. II. The standard deviation of the shadowing process is 3.4 dB and the correlation distance is 4.8 m.

### C. Correlation of PDP

We also evaluate the similarity of the omni-directional PDP  $\bar{P}_{h,\max}(i, \tau)$  measured along the continuous RX route, according to

$$X_{\text{pdp}}(i, j) = \frac{\int_{\tau} \bar{P}_{h,\max}(i, \tau) \bar{P}_{h,\max}(j, \tau) d\tau}{\sqrt{\int_{\tau} |\bar{P}_{h,\max}(i, \tau)|^2 d\tau} \sqrt{\int_{\tau} |\bar{P}_{h,\max}(j, \tau)|^2 d\tau}} \quad (11)$$

We can easily verify that  $X_{\text{pdp}}(i, i) = 1, \forall i$ . The analysis is similar to the one presented in [12] for the collinearity of PDP or local scattering function (LSF) in vehicle-to-vehicle propagation channels at 5.8 GHz. Fig. 4 presents the collinearity function of the PDP for the LoS route, where the same function is evaluated for LoS to NLoS transition route 2 in Fig. 5. If we set the threshold of de-correlation for  $X_{\text{pdp}}(i, j)$  as 0.9, the average correlation distance is about 0.9 m for the LOS scenario, but it can be as high as 4 m at the beginning section of the transition route and drops to about 1.26 m afterwards. These are comparatively smaller than the values presented in [12]. For the LoS case, the short correlation distance is a consequence of the high delay resolution, as the LoS moves from one resolvable delay bin to another with a relatively short movement of the RX. This has important consequences for the design of loop bandwidth in timing acquisition/tracking.

### D. Analysis with time-varying APS

We also analyze the time-varying angular power spectrum (APS) for both TX and RX along the two routes. The results provide important insight into the directional information about dominant multipath components (MPCs) when the RX

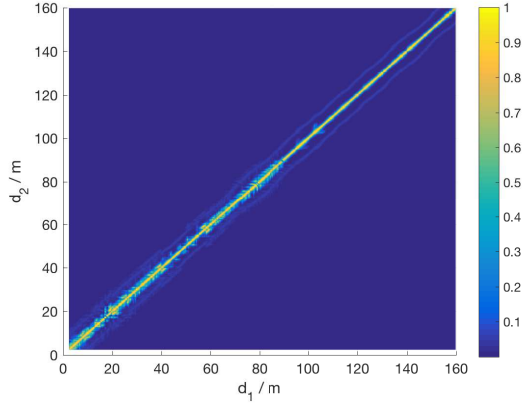


Fig. 4. The collinearity function of PDP for the LoS route

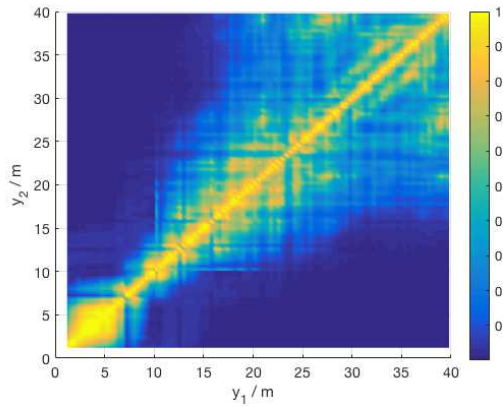


Fig. 5. The collinearity function of PDP for the LoS to NLoS route 2, when RX faces TX

moves along a continuous track. Similar to the definition in [18], we can compute the APS based on the average PDP from Eq. (2), which is given by

$$P(\varphi_T, d_i) = \sum_{n, \tau \in S_\tau^{m, n, i}} \bar{P}_h(m, n, i, \tau) \quad (12)$$

$$P(\varphi_R, d_i) = \sum_{m, \tau \in S_\tau^{m, n, i}} \bar{P}_h(m, n, i, \tau) \quad (13)$$

Here  $\varphi_T$  is the azimuth direction of departure (DoD) and ranges between  $-45^\circ$  and  $45^\circ$  with a  $5^\circ$  angle increment. Similarly we have  $\varphi_R$  for the azimuth direction of arrival (DoA). The directions of  $0^\circ$  in both cases are aligned with the orientations for TX and RX orientations. More details are presented in Section II. Figs. 6 and 7 are for the LoS route, where we can match the dominant direction with LoS. Figs. 8 and 9 are for the LoS to NLoS transition route, where we clearly see the dominant paths shift towards  $-40^\circ$  when RX moves into NLoS region. They are most likely reflected and diffracted paths around the street corner. This adaptation of the beam direction is critical for beam tracking, and depending on the speed of the TX/RX, relatively quick determination of new

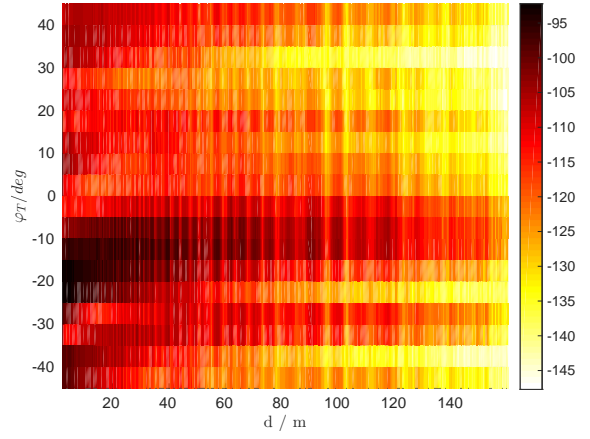


Fig. 6. The APS for TX on the LoS route

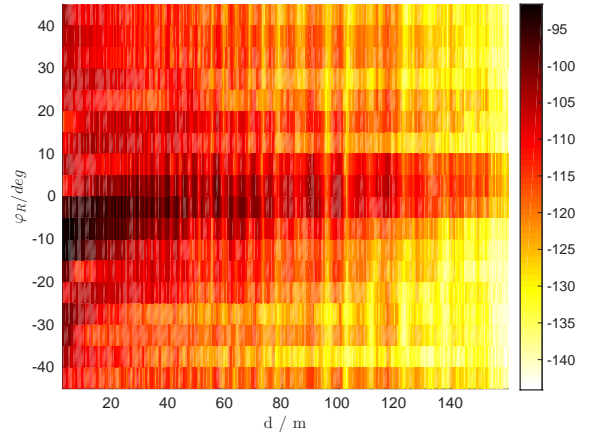


Fig. 7. The APS for RX on the LoS route

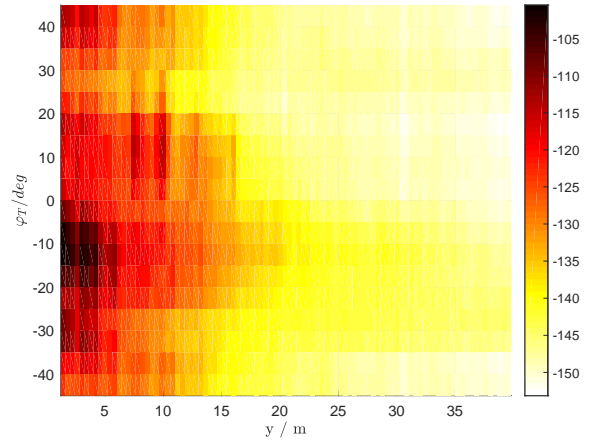


Fig. 8. The APS for TX on the LoS to NLoS transition route, when RX faces  $0^\circ$

directions would have to be taken into account. These changes occur at *both* the TX and the RX.

#### IV. CONCLUSION

In this paper we present, to our knowledge, the first extensive measurement results on the stationarity region of



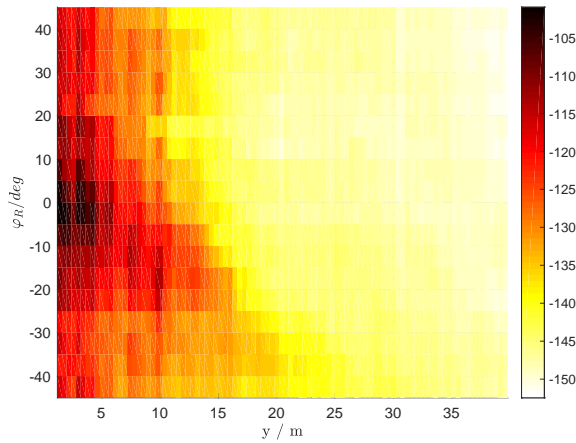


Fig. 9. The APS for RX on the LoS to NLoS transition route, when RX faces  $0^\circ$

MIMO mm-wave channels, which are based on over 20 million measured channel impulse responses. We have found that the foliage effect can significantly alter the PL exponent even in the LoS scenario, which leads the channel nonstationarity captured by our proposed dual-slope PL model. Meanwhile the propagation loss increases rapidly, about 30 dB, during the transition from LoS to NLoS scenario. We propose to model it with a street-by-street PL model. The autocorrelation distance of shadowing is 1.2 m in LoS route, although this value might be affected by the signal variation observed in the two-path channel. It rises up to 4.8 m for the LoS to NLoS transition route. The average correlation distance, computed based on the similarity of PDP, is 0.9 m for the LoS route. It can reach as high as 4 m at the beginning section of the transition route and drops to about 1.26 m afterwards. The analysis based on the correlation of shadowing and PDP has suggested that mm-wave channels exhibit a smaller stationarity region compared with cm-wave channels.

#### ACKNOWLEDGMENT

Part of this work was supported by grants from the National Science Foundation. The authors would like to thank Dr. Dimitris Psychoudakis, Thomas Henige, Robert Monroe for their contribution in the development of the channel sounder.

#### REFERENCES

- [1] J. G. Andrews, S. Buzzi, W. Choi, S. V. Hanly, A. Lozano, A. C. Soong, and J. C. Zhang, "What will 5g be?" *IEEE Journal on selected areas in communications*, vol. 32, no. 6, pp. 1065–1082, 2014.
- [2] S. Rangan, T. S. Rappaport, and E. Erkip, "Millimeter-wave cellular wireless networks: Potentials and challenges," *Proceedings of the IEEE*, vol. 102, no. 3, pp. 366–385, 2014.
- [3] A. F. Molisch, *Wireless communications*. IEEE Press - Wiley, 2011.
- [4] M. Shafi, A. F. Molisch, P. J. Smith, T. Haustein, P. Zhu, P. De Silva, F. Tufvesson, A. Benjebbour, and G. Wunder, "5g: A tutorial overview of standards, trials, challenges, deployment and practice," *IEEE Journal on Selected Areas in Communications*, 2017.
- [5] P. F. Smulders, "Statistical characterization of 60-ghz indoor radio channels," *IEEE Transactions on Antennas and Propagation*, vol. 57, no. 10, pp. 2820–2829, 2009.
- [6] K. Haneda, "Channel models and beamforming at millimeter-wave frequency bands," *IEICE Transactions on Communications*, vol. 98, no. 5, pp. 755–772, 2015.
- [7] A. Maltsev, R. Maslennikov, A. Sevastyanov, A. Lomayev, A. Khoryaev, A. Davydov, and V. Ssorin, "Characteristics of indoor millimeter-wave channel at 60 ghz in application to perspective wlan system," in *Proceedings of the Fourth European Conference on Antennas and Propagation*, April 2010, pp. 1–5.
- [8] K. Haneda, J. Zhang, L. Tan, G. Liu, Y. Zheng, H. Asplund, J. Li, Y. Wang, D. Steer, C. Li *et al.*, "5g 3gpp-like channel models for outdoor urban microcellular and macrocellular environments," in *Vehicular Technology Conference (VTC Spring), 2016 IEEE 83rd*. IEEE, 2016, pp. 1–7.
- [9] M. K. Samimi, G. R. MacCartney, S. Sun, and T. S. Rappaport, "28 ghz millimeter-wave ultrawideband small-scale fading models in wireless channels," in *Vehicular Technology Conference (VTC Spring), 2016 IEEE 83rd*. IEEE, 2016, pp. 1–6.
- [10] W. Roh, J.-Y. Seol, J. Park, B. Lee, J. Lee, Y. Kim, J. Cho, K. Cheun, and F. Aryanfar, "Millimeter-wave beamforming as an enabling technology for 5g cellular communications: theoretical feasibility and prototype results," *IEEE Communications Magazine*, vol. 52, no. 2, pp. 106–113, 2014.
- [11] G. Matz, "On non-wssus wireless fading channels," *IEEE Transactions on Wireless Communications*, vol. 4, no. 5, pp. 2465–2478, 2005.
- [12] A. Paier, T. Zemen, L. Bernado, G. Matz, J. Karedal, N. Czink, C. Dumard, F. Tufvesson, A. F. Molisch, and C. F. Mecklenbrauker, "Non-wssus vehicular channel characterization in highway and urban scenarios at 5.2 ghz using the local scattering function," in *Smart Antennas, 2008. WSA 2008. International ITG Workshop on*. IEEE, 2008, pp. 9–15.
- [13] R. He, O. Renaudin, V.-M. Kolmonen, K. Haneda, Z. Zhong, B. Ai, and C. Oestges, "Characterization of quasi-stationarity regions for vehicle-to-vehicle radio channels," *IEEE Transactions on Antennas and Propagation*, vol. 63, no. 5, pp. 2237–2251, 2015.
- [14] B. N. Liya and D. G. Michelson, "Characterization of multipath persistence in device-to-device scenarios at 30 ghz," in *Globecom Workshops (GC Wkshps), 2016 IEEE*. IEEE, 2016, pp. 1–6.
- [15] G. R. MacCartney Jr, H. Yan, S. Sun, and T. S. Rappaport, "A flexible wideband millimeter-wave channel sounder with local area and nlos to los transition measurements," *arXiv preprint arXiv:1703.08043*, 2017.
- [16] S. Sun, H. Yan, G. R. MacCartney Jr, and T. S. Rappaport, "Millimeter wave small-scale spatial statistics in an urban microcell scenario," *arXiv preprint arXiv:1703.08239*, 2017.
- [17] T. S. Rappaport, G. R. MacCartney Jr, S. Sun, H. Yan, and S. Deng, "Small-scale, local area, and transitional millimeter wave propagation for 5g communications," *arXiv preprint arXiv:1707.07816*, 2017.
- [18] C. U. Bas, R. Wang, D. Psychoudakis, T. Henige, R. Monroe, J. Park, J. Zhang, and A. F. Molisch, "A Real-Time Millimeter-Wave Phased Array MIMO Channel Sounder," *arXiv preprint arXiv:1703.05271*, 2017.
- [19] M. Friese, "Multitone signals with low crest factor," *Communications, IEEE Transactions on*, vol. 45, no. 10, pp. 1338–1344, 1997.
- [20] S. Hur, Y.-J. Cho, J. Lee, N.-G. Kang, J. Park, and H. Benn, "Synchronous channel sounder using horn antenna and indoor measurements on 28 ghz," in *Communications and Networking (BlackSeaCom), 2014 IEEE International Black Sea Conference on*. IEEE, 2014, pp. 83–87.
- [21] A. F. Molisch, A. Karttunen, S. Hur, J. Park, and J. Zhang, "Spatially consistent pathloss modeling for millimeter-wave channels in urban environments," in *2016 10th European Conference on Antennas and Propagation (EuCAP)*, April 2016, pp. 1–5.
- [22] S. Wyne, A. P. Singh, F. Tufvesson, and A. F. Molisch, "A statistical model for indoor office wireless sensor channels," *IEEE Transactions on Wireless Communications*, vol. 8, no. 8, 2009.